AGU PUBLICATIONS

JGR

Journal of Geophysical Research: Atmospheres

RESEARCH ARTICLE
10.1002/2016JD025116

Key Points:
- U.S. warm-West/cool-East dipole events associated with large circulation anomalies across the Northern Hemisphere mid-latitudes
- Historical increase in dipole events linked to increasing frequency of events when associated circulation patterns occur
- Positive trend in dipole events attributable to historical anthropogenic warming, though future warming is likely to reverse trend

Supporting Information:
- Supporting Information S1

Correspondence to:
D. Singh,
dsingh@ldeo.columbia.edu

Citation:
Singh, D., D. L. Swain, J. S. Mankin, D. E. Horton, L. N. Thomas, B. Rajaratnam, and N. S. Diffenbaugh (2016), Recent amplification of the North American winter temperature dipole, *J. Geophys. Res. Atmos.*, *121*, 9911–9928, doi:10.1002/2016JD025116.

Received 18 MAR 2016
Accepted 30 JUL 2016
Accepted article online 4 AUG 2016
Published online 1 SEP 2016

Recent amplification of the North American winter temperature dipole

Deepti Singh[1,2], Daniel L. Swain[1], Justin S. Mankin[2,3], Daniel E. Horton[1,4,5], Leif N. Thomas[1], Bala Rajaratnam[1,6], and Noah S. Diffenbaugh[1,5]

[1]Department of Earth System Science, Stanford University, Stanford, California, USA, [2]Lamont-Doherty Earth Observatory, Columbia University, Palisades, New York, USA, [3]NASA Goddard Institute for Space Studies, New York, New York, USA, [4]Department of Earth and Planetary Sciences, Northwestern University, Evanston, Illinois, USA, [5]Woods Institute for the Environment, Stanford University, Stanford, California, USA, [6]Department of Statistics, Stanford University, Stanford, California, USA

Abstract During the winters of 2013–2014 and 2014–2015, anomalously warm temperatures in western North America and anomalously cool temperatures in eastern North America resulted in substantial human and environmental impacts. Motivated by the impacts of these concurrent temperature extremes and the intrinsic atmospheric linkage between weather conditions in the western and eastern United States, we investigate the occurrence of concurrent "warm-West/cool-East" surface temperature anomalies, which we call the "North American winter temperature dipole." We find that, historically, warm-West/cool-East dipole conditions have been associated with anomalous mid-tropospheric ridging over western North America and downstream troughing over eastern North America. We also find that the occurrence and severity of warm-West/cool-East events have increased significantly between 1980 and 2015, driven largely by an increase in the frequency with which high-amplitude "ridge-trough" wave patterns result in simultaneous severe temperature conditions in both the West and East. Using a large single-model ensemble of climate simulations, we show that the observed positive trend in the warm-West/cool-East events is attributable to historical anthropogenic emissions including greenhouse gases, but that the co-occurrence of extreme western warmth and eastern cold will likely decrease in the future as winter temperatures warm dramatically across the continent, thereby reducing the occurrence of severely cold conditions in the East. Although our analysis is focused on one particular region, our analysis framework is generally transferable to the physical conditions shaping different types of extreme events around the globe.

1. Introduction

Simultaneous occurrence of extreme climate events in adjacent regions can exacerbate impacts on the economy, natural resources, and emergency services. Understanding the causes of such extremes can inform disaster preparation, early warning, and risk management systems.

The winters of 2013–2014 and 2014–2015 were characterized by severe meteorological events that had wide-ranging impacts across sectors in North America [*NOAA*, 2015]. Much of the western U.S. experienced exceptionally warm and dry conditions that aggravated the region's extraordinary multi-year drought [*Diffenbaugh et al*., 2015]. Persistent warm temperatures [*Griffin and Anchukaitis*, 2014] were accompanied by record-low soil moisture and mountain snowpack, increasing wildfire risk [*Yoon et al*., 2015] and reducing water availability for agriculture, ecosystems, and urban areas. The central and eastern U.S., meanwhile, experienced frequent cold Arctic air outbreaks and intense winter storms. Associated heavy snowfalls and blizzard conditions crippled transportation infrastructure and disrupted the economies of several major American cities, particularly along the Eastern Seaboard [*Bacon*, 2015]. Insured losses in the 2014–2015 winter amounted to 2.4 billion USD, double the average of the last decade [*Yoon et al*., 2015].

These contrasting "warm-West/cool-East" conditions have been linked by a well-defined pattern of anomalous atmospheric circulation extending over a large portion of the Northern Hemisphere mid-latitudes [*S.-Y. Wang et al*., 2015]. Land-sea contrasts and the mountainous topography of the western U.S. influence the position and amplitude of the climatological mid-tropospheric wave pattern, which in winter exhibits a mean ridge along the West Coast and a mean trough near the Eastern Seaboard [*Blackmon et al*., 1977]. The atmospheric pattern associated with the warm-West/cool-East events represents an amplification of this

climatological mean winter state, with an anomalous mid-tropospheric ridge extending over western North America, Alaska, and the Arctic, and a downstream mid-tropospheric trough over the central and eastern U.S.

Several teleconnections have been invoked to explain the unusual atmospheric circulation pattern linked to these winter surface temperature extremes, including unusual variability of tropical western Pacific sea surface temperatures [*Ding et al*., 2014; *Wang et al*., 2014; *Hartmann*, 2015], the decline of Arctic sea ice [*Handorf et al*., 2015; *Kug et al*., 2015; *Lee et al*., 2015; *Overland et al*., 2015], and enhanced autumn snow cover in Eurasia [*Cohen et al*., 2013; *Furtado et al*., 2015; *Handorf et al*., 2015].

The first mechanism involves enhanced ridging in the northeastern Pacific and western U.S. (and subsequent downstream troughing over eastern North America) due to the poleward propagation of Rossby waves originating from a region of persistent tropospheric heating anomalies in the western tropical Pacific [*Ding et al*., 2014; *Wang et al*., 2014; *Hartmann*, 2015]. In the second mechanism, extensive sea ice loss in the Barents-Kara Sea and/or East Siberian-Chukchi Sea regions weakens the polar jet stream by decreasing the poleward temperature gradient in certain sectors, perhaps increasing the "waviness" of midlatitude flow patterns (including the ridge/trough pattern over North America) [*Petoukhov et al*., 2013; *Cohen et al*., 2014]. Sea ice loss also warms the atmospheric layers (1000–500 mb) and increases the heights of pressure surfaces locally, contributing to the decrease in the thickness gradient that further weakens the strength of the jet stream [*Vihma*, 2014]. Both of these effects might allow for more frequent cold air outbreaks and more persistent extreme weather patterns [*Overland et al*., 2015, and references therein]. In the third mechanism, enhanced Eurasian snow cover advance/extent in October forces a negative North Atlantic Oscillation (NAO)-like response in the Northern Hemisphere wintertime circulation via a series of complex stratospheric-tropospheric interactions [*Furtado et al*., 2015, 2016; *Handorf et al*., 2015], ultimately causing a southward shift of the upstream polar jetstream over North America [*Kug et al*., 2015; *Lee et al*., 2015].

Together, these hypotheses highlight potential linkages between land, ice, and/or ocean forcings and seasonal-scale circulation patterns that strongly resemble the 2013–2014 and 2014–2015 winters. Any true physical linkage between these forcings and short-duration temperature extremes over North America would likely involve interplay between the seasonal circulation and more transient, higher-frequency meteorological processes. However, few studies have examined the characteristics and evolution of daily-scale extreme warm-West/cold-East dipole events over North America. Further, most previous observational studies have focused separately upon the causes of either the persistent ridge in the West [*Wang et al*., 2014; *Hartmann*, 2015] or the anomalous trough in the East [*Cohen et al*., 2013; *Handorf et al*., 2015; *Kug et al*., 2015], rather than considering their simultaneous occurrence.

Given the potential for dynamical linkages between the warm-West/cool-East events via the background atmospheric circulation state, we investigate the phenomenon of co-occurring daily-scale extremes as a coherent entity, which we refer to as the "North American winter temperature dipole" ("NAWTD") (Figure 1). In doing so, we present the first characterization of these daily-scale surface extremes, their associated middle atmospheric configuration, and their response to radiative forcing changes. We first develop a metric to capture the magnitude and spatial extent of these co-occurring NAWTD temperature extremes. We then quantify the long-term trends in the NAWTD surface temperature metrics and investigate relationships between those trends and changes in mid-tropospheric circulation patterns. Finally, we consider whether anthropogenic forcing has influenced the likelihood of observed changes in NAWTD frequency and intensity.

2. Data and Methods

2.1. Data Sets

We use daily 2-m maximum and minimum air temperatures and geopotential heights from the National Centers for Environmental Prediction/National Center for Atmospheric Research Reanalysis 1 (NCEP/NCAR R1) data set [*Kalnay et al*., 1996] to study daily-scale temperature extremes and their associated circulation patterns. These data are available at a spatial resolution of 2.5° from 1948 to present (http://www.esrl.noaa.gov/psd/). Our analysis focuses on the 1980–2015 period in order to allow for a direct comparison between the reanalysis- and observation-based temperature metrics, while restricting our analysis of atmospheric circulation patterns to the postsatellite era [*Horton et al*., 2015].

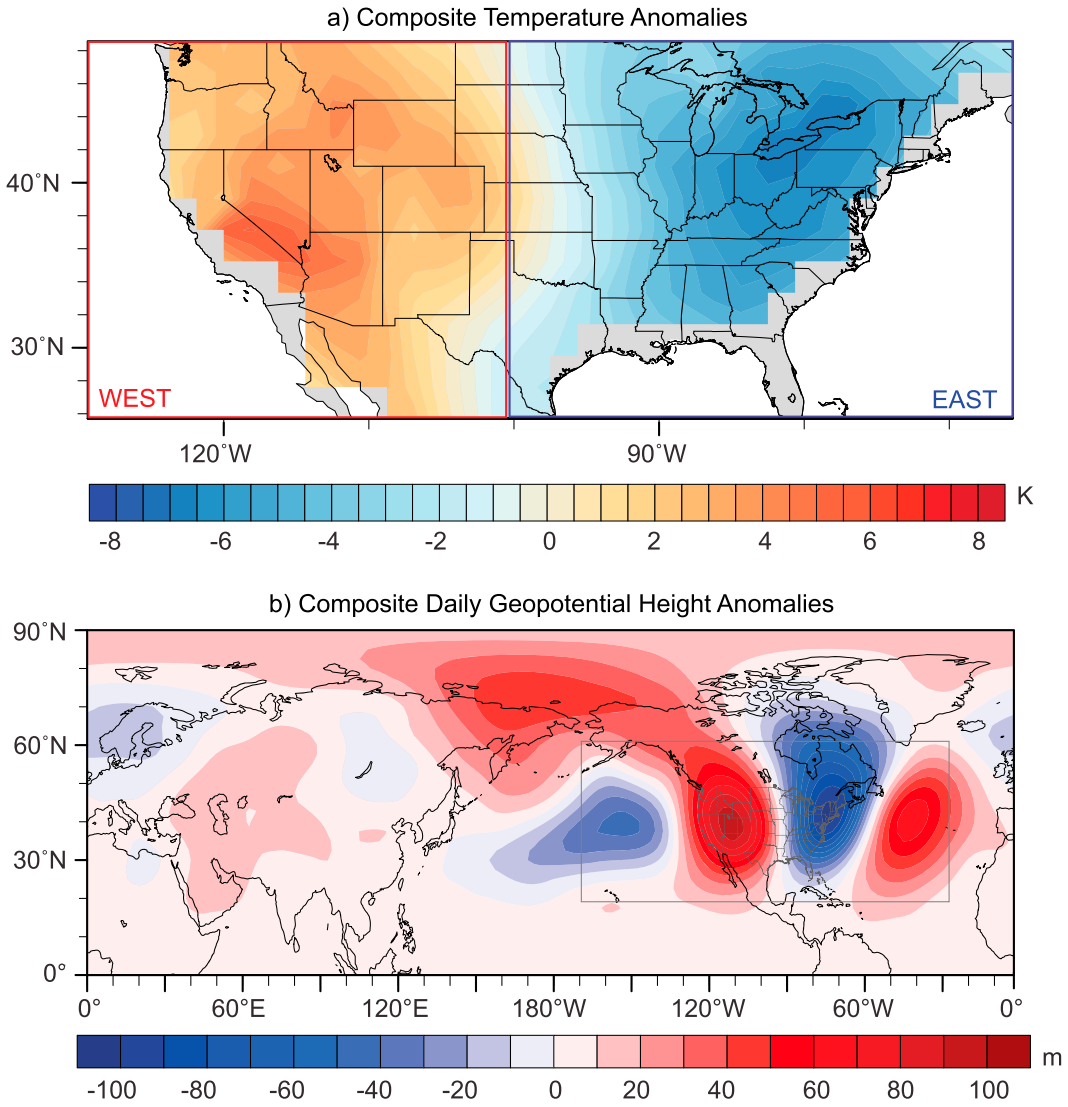

Figure 1. North American winter temperature dipole (NAWTD): Observed composites of (a) near-surface (2 m) temperature anomalies and (b) mid-tropospheric (500mb) geopotential height anomalies for all historical (1980–2015) winter temperature dipole event occurrences defined using a 15% geographic area threshold. The eastern and western dipole regions are defined in Figure 1a, while the circulation analysis domain is outlined by the grey box in Figure 1b. Here we define a daily dipole event to be the co-occurrence of (1) daily maximum temperatures over 15% or more of the western domain's land grid cells greater than their 84th percentile threshold and (2) daily minimum temperatures over 15% or more of the eastern domain's land grid cells less than their 16th percentile threshold.

To maintain physical consistency with atmospheric variables used to identify circulation patterns (section 2.3), we primarily use temperature and geopotential heights from the reanalysis data set. However, we test the sensitivity of the trends in temperature extremes by using other data sets, including ground-based instrumental measurements. These include the high-resolution (32 km) North American Regional Reanalysis data set and two instrumental data sets—Oregon State University's Parameter-elevation Relationships on Independent Slopes Model (PRISM) product [*Parameter-elevation Relationships on Independent Slopes Model*, 2015] and the University of Idaho's Meteorological (METDATA) data set [*Abatzoglou*, 2013], both of which have a spatial resolution of 4 km (Figure S1 in the supporting information). Whereas PRISM is based on the network of ground-based observations, METDATA combines the monthly scale PRISM data set with some variables from regional-scale reanalysis products to produce a spatially and temporally consistent data set.

To assess whether the observed trends in NAWTD events occurred purely by chance or were influenced by historical forcings, we analyze pre-industrial and historical simulations from the NCAR's Large Ensemble climate model experiment ("LENS")[*Kay et al*., 2014]. The LENS single-model ensemble is designed to simulate internal (or "natural") climate variability by running many realizations of a single model, with the realizations differing only in slight perturbations of the initial atmospheric conditions [*Kay et al*., 2014]. LENS was run with the CESM1 coupled global climate model, with ~1° horizontal resolution in the atmospheric component (Community Atmosphere Model version 5). At the time of data acquisition, 35 ensemble members were available. The 35 historical ("HIST") realizations have identical radiative forcing for the 1920–2005 period but are initialized with slightly different atmospheric conditions. The 35 future realizations are extensions of the respective 35 HIST realizations, but with the Representative Concentration Pathway (RCP) 8.5 forcing applied for the 2006–2100 period. An 1800-year long, single-realization simulation with constant pre-industrial forcings ("PIcontrol") was available for the control case. The long PIcontrol simulation provides an opportunity to examine internal variability in a climate that is unaffected by changes in climate forcing factors.

2.2. Temperature Extremes

We calculate daily temperature extremes at each grid point based on exceedances of a percentile threshold that is derived from the distribution of all days within the winter season (December-January-February (DJF)) during the baseline period (defined as 1980–2000; see above). This threshold is defined at each grid point as the 84th percentile of the winter daily maximum temperature distribution for warm extremes and the 16th percentile of the winter daily minimum temperature distribution for cold extremes. The 84th/16th percentiles approximate ±1 standard deviation of a Gaussian distribution. Prior to calculating the respective temperature thresholds, we remove the linear warming/cooling trend in the time series of daily maximum and minimum temperatures [*Lee et al*., 2014] to avoid biasing the thresholds toward earlier or later periods of the record.

To describe the spatial characteristics of the warm-West/cool-East surface temperature anomaly pattern, we divide the U.S. into two domains, approximately separated by the eastern edge of the Rockies: West (25–50°N, 130–103°W) and East (25–50°N, 103–65°W). The eastern edge of the Rocky Mountains acts as a physically influential topographical barrier, often separating air masses of very different character, and also aligns closely with the central divide of the warm-West/cool-East temperature dipole observed in 2013–2014 and 2014–2015 (Figure 1a). We define a NAWTD event as a day with simultaneously occurring warm extremes (daily maximum temperatures $>$ 84th percentile) in the West and cold extremes (daily minimum temperatures $<$ 16th percentile) in the East over a minimum geographic fraction of the land grid points. We examine NAWTD events with fractions of the minimum geographical areas within each domain simultaneously experiencing extremes ranging from 5% to 30% (Figure 2). (By definition, dipole events over higher geographic fractions of the land grid points are included in the counts of dipole events defined over lower geographic fractions.) We define NAWTD intensity as the difference in area-weighted average temperatures of the West and East domains experiencing warm/cold extremes.

Although the occurrence of extremes in either region has important consequences, our analysis focuses on extremes that occur in both regions simultaneously, as these are likely to have greater national-scale impacts and impose greater stress on disaster management efforts. Further, the specific warm-West/cold-East configuration represents an amplification of the seasonal-mean winter configuration, which is a possible mechanism by which global warming could increase the probability of both extremely warm and extremely cold midlatitude events.

2.3. Clustering of Atmospheric Circulation Patterns

To identify the circulation patterns associated with NAWTD events, we use mid-tropospheric (500 mb) geopotential height anomalies from the NCEP-NCAR R1. Using Self-Organizing Maps (SOMs) [*Kohonen*, 2001; *Johnson*, 2013; *Horton et al*., 2015], we categorize the 1980–2015 daily winter (DJF) geopotential height anomalies over the domain of interest into a predefined number of topologically ordered representative clusters (or "nodes"; Figure S2) [*Kohonen*, 2001]. Daily circulation patterns are binned into clusters by minimizing the Euclidean distance between the iteratively updated cluster composites and the daily geopotential height anomalies on all matching days included in those clusters. We restrict the SOM circulation analysis to the domain that encompasses the approximate spatial extent of the anomalous circulation pattern observed during 2013–2014 and 2014–2015 (i.e., 25–60°N and 190–330°E; Figure 1b). Geopotential height anomalies

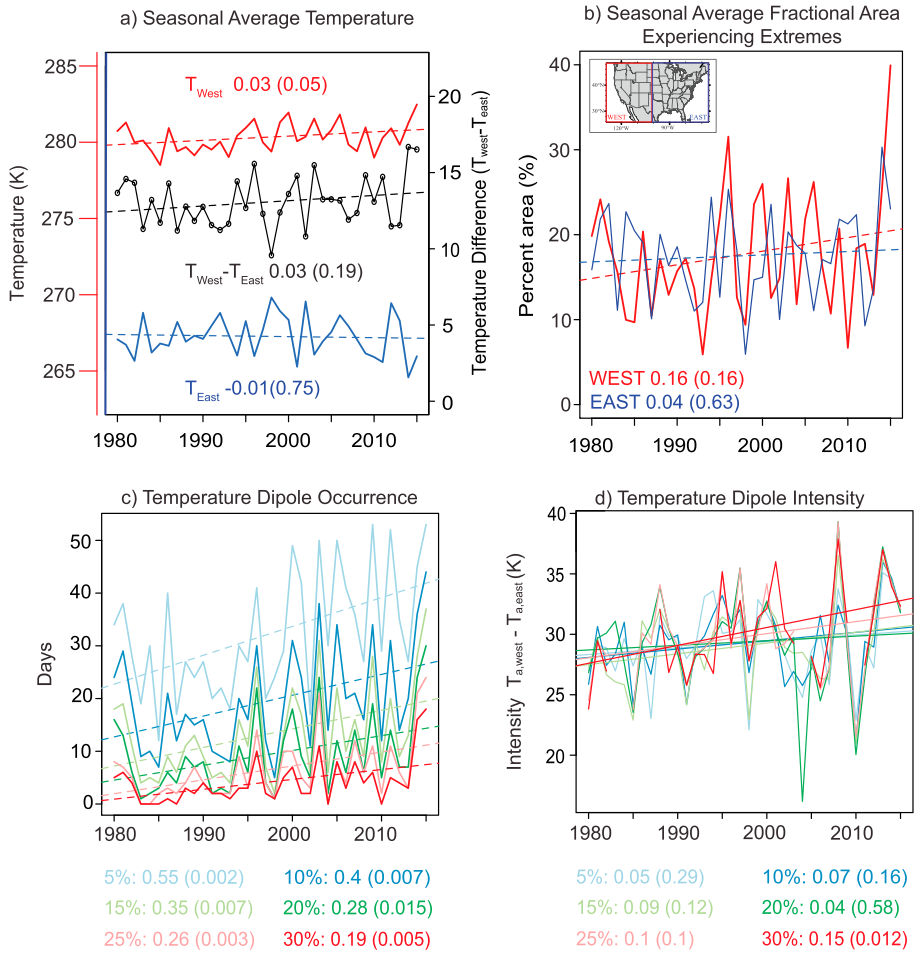

Figure 2. North American winter temperature dipole (NAWTD) characteristics: Time series (1980–2015) of (a) seasonal average of daily maximum/minimum temperatures in the western and eastern U.S. domains (left axis) and their difference (right axis), (b) seasonal average fractional area of western/eastern domains experiencing warm/cool extremes, (c) temperature dipole occurrence, and (d) seasonal average temperature dipole intensity. Dipole intensity is defined as the difference in area-weighted average temperature between the western ($T_{a,west}$) and eastern ($T_{a,east}$) domain for all grid cells exceeding the extreme thresholds. Colors in Figures 2c and 2d represent the minimum land fractions experiencing extremes used to define the dipole events. The numbers in Figures 2a and 2b and below Figures 2c and 2d indicate the linear trend magnitudes and their statistical significance in brackets.

are calculated by removing the calendar-day mean at each grid point. To reduce the influence of high-frequency variability on the seasonal cycle, daily data are smoothed by using a low-pass filter [*Holloway*, 1958] with a cut-off period of 21 days following [*Feldstein*, 2000; *Franzke et al.*, 2011], prior to the calculation of the calendar day mean. The filtering scheme iteratively calculates a weighted average value for that day by using days preceding and following the calendar day, with the number of iterations determined by the cutoff period.

Previous studies have proposed different criteria for selecting the number of nodes for clustering based on the significance of the patterns [*Johnson*, 2013; *Singh et al.*, 2014a; *Dawson and Palmer*, 2015]. However, there is no universally accepted method for this selection [*Bao and Wallace*, 2015; *Horton et al.*, 2015], largely because the suitability of the number of nodes varies depending on the application. Rare atmospheric patterns are unlikely to be captured with a small number of nodes, whereas a large number of nodes can result in substantial similarity between patterns [e.g., *Horton et al.*, 2015]. Therefore, selecting the number of nodes requires a balance between having a sufficiently large number of nodes to capture rare configurations and having a sufficiently small number to maintain distinction between the patterns [*Bao and Wallace*, 2015].

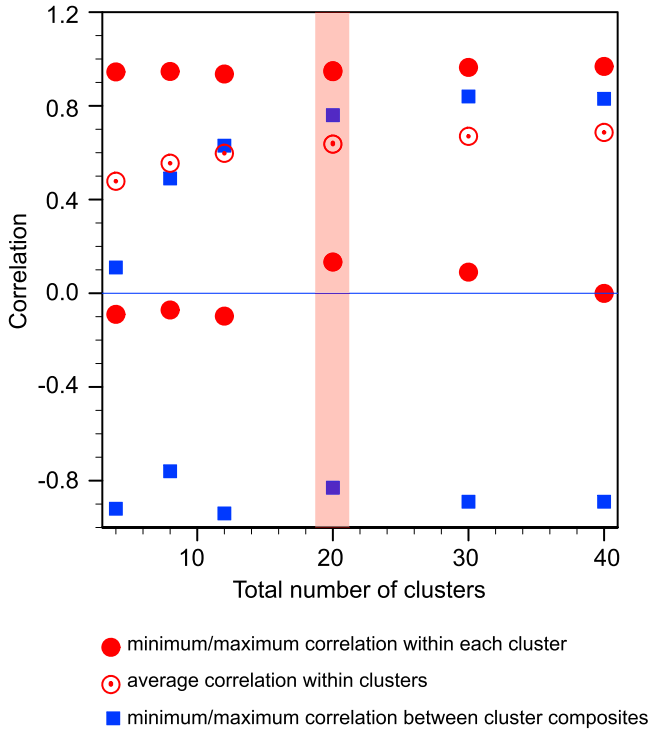

Figure 3. Determining the number of SOM clusters: An optimal number of clusters is determined by assessing spatial correlations between the circulation patterns within clusters and between clusters. Here average, minimum, and maximum spatial correlations between daily circulation patterns and their corresponding composite cluster patterns are plotted in red. Minimum and maximum correlations between the cluster composite patterns are shown in blue. We highlight (red box) the number of clusters (here 20) that ensures all days are positively correlated with their corresponding cluster composite and the within-cluster variance in correlations is minimized.

We assess the suitability of the number of clusters by using the spatial correlations between the daily geopotential height anomalies and the composite pattern of their corresponding cluster (i.e., the "within-cluster correlation") (Figure 3). The suitability of the number of clusters is based on maximizing the average within-cluster correlations, while ensuring that the pattern on all days is positively correlated with its cluster composite. We performed the SOM clustering with multiple node numbers: 4, 8, 12, 20, 30, and 40 for geopotential height anomalies over the domain (25–60°N and 190–330°E; Figure 1b). The average within-cluster correlation increases slightly with larger number of nodes. With fewer than 20 nodes, the minimum within-cluster correlation falls below zero, likely due to the large number of days that are being composited into a limited number of clusters. In contrast, the minimum within-cluster correlation is greater than zero for both 20 and 30 nodes and is equal to zero for 40 nodes. Because the minimum correlation is slightly higher with 20 nodes than with 30 nodes, and a smaller number of nodes are generally more desirable to reduce the correlation between the different clusters, we select a 20-node SOM to perform our analysis. The 20-node SOM has a sufficiently large number of clusters that all underlying patterns are positively correlated with each cluster composite (Figure 3), and the cluster is able to capture the pattern resembling the one associated with NAWTD events (Figures 1 and 4).

Since we examine changes in the temporal characteristics of these nodes, there is a concern that uniform thermal expansion of the troposphere caused by recent global-scale warming could create spurious trends in pattern occurrence [*Horton et al.*, 2015]. Some previous studies have therefore removed the local, domain-averaged, or hemispheric trend [*Driouech et al.*, 2010; *Cattiaux et al.*, 2013; *Horton et al.*, 2015] in geopotential heights from each grid point to account for this effect. However, it has been recently shown that the thermal dilation of the troposphere over the recent decades is spatially heterogeneous, particularly over the North Pacific sector [*Horton et al.*, 2015; *Swain et al.*, 2016]. Due to this spatial heterogeneity in the historical trends, we elect not to remove the local, regional, and hemispheric trends in geopotential heights for the period of analysis.

Using the SOM categorization of atmospheric patterns, we analyze different characteristics of these clusters, including their frequency of occurrence within the winter season. Since each day's circulation pattern has been binned in a specific cluster, we can further match the atmospheric patterns on days with NAWTD surface temperature occurrences with these SOM clusters. Using this information, we calculate the number of NAWTD occurrences associated with each representative cluster over the length of the record, as well as temporal trends in the number and fraction of total NAWTD event occurrences associated with each pattern.

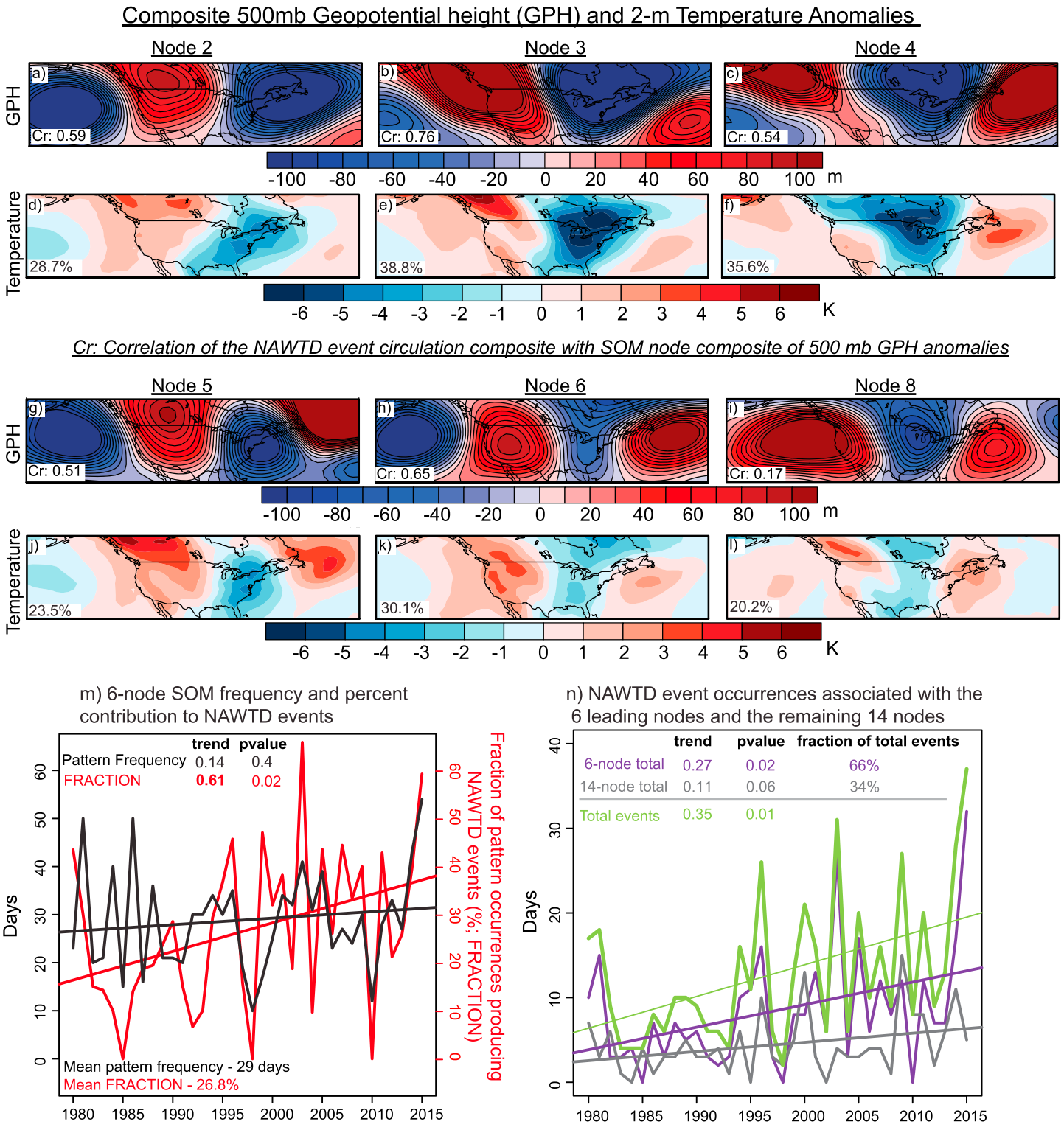

Figure 4. Related circulation trends: (a–c and g–i) Composite winter (DJF) mid-tropospheric geopotential height anomalies and (d–f and j–l) corresponding near-surface temperature anomalies for six of the 20 SOM cluster patterns (see Figure S2 for all cluster composites). We display the six leading patterns with the highest spatial correlation (C_r) to the (15% minimum area) NAWTD event geopotential height composite (Figure 1b). Percentages in Figures 4d–4f and 4j–4l indicate the fraction of SOM occurrences that are associated with NAWTD events at the surface. These six patterns collectively account for 66% of all NAWTD events. (m) Time series of occurrence of the six SOM nodes (sum) and the fraction of these six SOM node occurrences that produce dipole events. (n) Time series of the total number of NAWTD events, dipole events associated with the six leading nodes, and dipole events associated with the remaining 14 nodes.

2.4. Quantification of Trends

We estimate trends in the frequency of NAWTD event occurrence, the frequency of SOM pattern occurrence, and the number and fraction of NAWTD events associated with each SOM pattern. Since the assumption of normality (which is a prerequisite for a linear regression model) is not met by these characteristics, we use a nonparametric bootstrapping approach to estimate trends and their significance by using linear least squares regression. Bootstrapping provides a more accurate estimate of the trend coefficients when the underlying sample size is small (as is the case in our analysis). We use 1000 bootstrap iterations to estimate the true regression coefficients. In each iteration, we bootstrap the residuals of the linear regression from the original time series to generate a new time series. We calculate the *t* statistic as a ratio of the original trend and the standard error calculated from the trend estimates of the bootstrapped time series, and then use the *t* distribution to calculate its significance. (We tested for temporal autocorrelation as in *Singh et al*. [2014b] and found no statistically significant autocorrelation in most time series.)

2.5. Trend Attribution

Using the LENS ensemble, we calculate the probability of the observed dipole trends in the historical and pre-industrial forcing regimes. To match the length of the observed record (1980–2015), we generate a distribution of 36-year trends from the 35 realizations in the LENS HIST simulations and from non-overlapping periods of the ~1800-year LENS pre-industrial control simulation. Since the historical simulations were only run through 2005, we select the 36-year period ending in 2005 (1970–2005). The PIcontrol distribution represents the range of trends from natural variability in the pre-industrial climate. The HIST distribution represents the response of the climate system to historical forcing superimposed on the range of natural variability.

We apply the Kolmogorov-Smirnov test to determine whether the distributions of trends in the HIST and PIcontrol are statistically distinguishable. Further, we assess whether the likelihood of the observed trend direction (positive or negative) is equal in these two climates or if instead global warming has influenced the likelihood of the trend direction. To do so, we use a binomial test to determine whether the likelihood of a specific trend direction occurring in the historical climate is similar to the likelihood expected from natural climate variability in an unperturbed climate. *P*-values from the binomial test indicate the level of significance of the difference in likelihoods between the two climates.

In quantifying this likelihood that internal variability would generate trends in a specific direction in the forced or unforced climate, we use the entire ensemble of trends independent of their significance. The significance of individual trends only indicates whether a particular trend is atypical but does not provide information about whether a positive or negative trend is not equally likely in both climates (refer to Table S1 in the supporting information for the fraction of significant trends). Rather, by considering the complete ensemble, our goal is to assess whether there are sufficiently enough positive trends to say that the assertion of equal probability of positive/negative trends in the two climates is rejected.

To estimate the likelihood of positive or negative trends in an unperturbed climate, we divide the 1800 year pre-industrial control simulation into nonoverlapping 36 year periods. The likelihood of positive or negative trends is defined as the proportion of these 49 nonoverlapping 36 year periods that have trends in the same direction as the observed trend. This empirically determined likelihood estimate is used to set the expected probability of positive or negative trends (depending on the observed trend direction) for the binomial distribution (p_o). Of the 35 identical ensemble members, we use this binomial distribution based on the pre-industrial probability to determine the probability (p_h) of the number of historical ensemble members (n_h) exhibiting a trend in the same direction as the observations.

We ask two specific questions to test whether the probabilities of positive or negative trends are significantly different in the historical and pre-industrial climates, and if so, whether the probability is greater in the direction of the observed trends in the historical climate with anthropogenic forcings relative to the pre-industrial climate. These questions are based on the following null hypothesis:

$$H0 : p_o = p_h$$

1. Of the 35 historical ensemble members, is the probability of *n* trends in the observed direction *significantly higher or significantly lower* than the expected value in a pre-industrial climate? The alternative hypothesis for this test is

$$H1 : p_o \neq p_h$$

A low *P*-value from this two-tailed binomial test indicates that we can reject the null hypothesis that the probability of positive or negative trends is similar in the pre-industrial and historical climates. This test does not indicate the direction in which the probability has changed.

2. Is the probability of a trend in the same direction as the observations *more* likely in the historical climate than in the pre-industrial control climate? The alternative hypothesis for this test is

$$H2 : p_h > p_o$$

A low *P*-value from this single-tailed binomial test indicates that it is unlikely that the proportion of historical trends in the observed direction occurred purely by natural variability and that historical warming has increased the probability of trends in the observed direction.

3. Results and Discussion

3.1. North American Winter Temperature Dipole (NAWTD) and its Associated Atmospheric Circulation Pattern

Figure 1a is a composite of the surface air temperature anomalies of all historical (1980–2015) dipole events defined with a minimum 15% geographical area threshold (i.e., at least 15% of the land area in the West was extremely warm and at least 15% of the land area in the East was extremely cold). Three quarters of these events have historically occurred in January (37%) or February (40%). During the 2013–2014 and 2014–2015 winters, North America frequently experienced a similar warm-West/cool-East surface temperature dipole pattern associated with notable daily-scale extremes [*Hartmann*, 2015; *S.-Y. Wang et al*., 2015]. In fact, the coolest Eastern winter and the warmest Western winters on record since at least 1980 occurred during 2013–2014 and 2014–2015, respectively—and the difference between West and East near-surface air temperatures therefore reached an observationally unprecedented magnitude during both 2013–2014 and 2014–2015 (Figure 2a). Further, in 2013–2014, the fraction of the eastern U.S. experiencing daily minimum temperatures below the historical 16th percentile reached its greatest value since at least 1980 (~28%; Figure 2b). Likewise, in 2014–2015, the fraction of the western U.S. experiencing daily maximum temperatures above the 84th percentile also reached its greatest value since at least 1980 (~40%; Figure 2b).

The composite structure of the mid-tropospheric (500 mb) geopotential height anomalies for all historical (1980–2015) NAWTD occurrences reveals a coherent large-scale circulation pattern over a large portion of the Northern Hemisphere (Figure 1b).

This circulation pattern includes an anomalous atmospheric wavetrain extending from the North Pacific eastward across the entire North American continent to the western North Atlantic, with an anomalous ridge over the western U.S. and an anomalous trough over the eastern U.S. (Figure 1b). The anomalous atmospheric ridge that displaces the midlatitude westerlies poleward [*Swain et al*., 2014] creates conditions suitable for anomalously warm temperatures in the western U.S. The anomalous downstream trough facilitates the advection of cold, polar air toward the central and eastern U.S. [*Vihma*, 2014], leading to increased occurrence of daily-scale cold extremes. Although the observed anomalies in the composite pattern are primarily restricted to the mid-latitudes, substantial positive geopotential height anomalies also extend as far north as the Arctic Ocean north of Alaska and into the subtropical North Atlantic.

3.2. Detection of Long-Term Trends in NAWTD Events

Given the changes that have occurred in Earth's climate in recent decades, including changes in remote forcings of North American winter climate [*Comiso et al*., 2008; *Cohen et al*., 2014; *Intergovernmental Panel on Climate Change*, 2013], we examine trends in the characteristics of NAWTD events (Figure 2). We find that the seasonal-scale west-east temperature difference exhibits an increasing trend (0.03 K/yr; *P*-value = 0.19) over the period of observation, primarily as a consequence of increasing temperatures

Table 1. Sensitivity of Trends to Extreme Winter Seasons: Comparison of Linear Trend Magnitudes and Their Significance in Seasonal and Extreme Winter (DJF) Temperature Characteristics Calculated Over the 1980–2015 Period and Over the 1980–2013 Period

Characteristic	1980-2015		1980-2013	
	trends	p-values	trends	p-values
Western U.S. Temperature	0.03	0.05	0.02	0.3
Eastern U.S. Temperature	-0.01	0.75	0.01	0.52
West-East Temperature Difference	0.03	0.2	-	-
Fraction Extreme Area West	0.16	0.16	0.02	0.8
Fraction Extreme Area East	0.04	0.64	-0.05	0.6
NAWTD Event Severity				
5% Events	0.05	0.3	0.02	0.7
10% Events	0.07	0.15	0.04	0.4
15% Events	0.09	0.1	0.06	0.3
20% Events	0.04	0.6	0.01	0.9
25% Events	0.1	0.12	0.08	0.3
30% Events	0.15	0.012	0.14	0.026
NAWTD Event Occurrence				
5% Events	0.55	0.002	0.46	0.01
10% Events	0.4	0.01	0.24	0.1
15% Events	0.35	0.007	0.21	0.09
20% Events	0.28	0.011	0.14	0.16
25% Events	0.26	0.003	0.14	0.08
30% Events	0.19	0.004	0.08	0.1

Significant at the 10% level over both 1980-2013 and 1980-2015 periods
Significant at the 10% level only over 1980-2015 period

The purple highlights characteristics that are significant at the 10% level over both 1980–2013 and 1980–2015. The orange highlights characteristics that are only significant at the 10% level over 1980–2015 period and have *P*-values > 0.1 over 1980–2013.

(0.03 K/year; *P*-value = 0.05) in the western domain and slightly decreasing temperatures (−0.01 K/year; *P*-value = 0.75) in the eastern domain (Figure 2a). Further, there is a substantial but statistically insignificant increasing trend (0.16%/year; *P*-value = 0.16) in the average fraction of the western domain experiencing warm extremes, but no discernible trend in the fraction of the eastern domain experiencing cold extremes (*P*-value = 0.63; Figure 2b).

The net effect of these observed trends is a large and statistically significant increase in the co-occurrence of warm-West/cool-East temperature extremes. These trends are statistically significant for all geographic thresholds (*P*-value < 0.02; Figure 2c), although the magnitude of the trend decreases for the larger-area events. In 2013–2014 and 2014–2015, the number of NAWTD events defined with the fractional area experiencing extremes exceeding 10% was among the highest observed since 1980. The magnitude of trends in NAWTD intensity also generally increases for increasing spatial extents, although only the trend for the most extreme events (30% area threshold) is significant at the 95% confidence level (*P*-value = 0.012; Figure 2d).

Based on both seasonal- and daily-scale measures, the winters of 2013–2014 and 2014–2015 were extreme in the observational record (Figure 2). Since these two extremes occur at the end of the observed time series, they could have a large influence on the detection of trends. We test the sensitivity of the observed trends to the inclusion of these 2 years (Table 1). A majority of the trends in dipole event occurrence remain significant at the 10% level even though the trend magnitudes are slightly lower. Indeed, we find that although the 2013–2014 and 2014–2015 seasons affect the magnitude of trends and their significance for some quantities, there were significant trends in dipole event occurrence even before these two recent extreme seasons. (The most notable exceptions are western U.S. temperatures and the intensity of 15% dipole events, for which the significance of trends drop from the 10% to the 30% confidence level without including the two extreme seasons.)

Table 2. Data Set Intercomparison: Magnitude of Linear Trends in Seasonal and Extreme Winter (DJF) Temperature Characteristics From the PRISM Climate Data, METDATA, and the North American Regional Reanalysis (NARR) Data Sets, and Their *P*-Values (in Grey)

	PRISM		METDATA		NARR	
Characteristic	Trend	*P*-value	Trend	*P*-value	Trend	*P*-value
Western U.S temp	0.03	0.17	−0.01	0.71	0	0.8
Eastern U.S temp	0.01	0.716	0.01	0.6	0.03	0.16
Fraction West	0.15	0.15	−0.12	0.24	−0.12	0.3
Fraction East	−0.09	0.4	−0.11	0.32	−0.16	0.16
NAWTD event severity						
5% events	0	0.99	−0.01	0.8	0.07	0.25
10% events	0	0.99	0.02	0.8	0.09	0.13
15% events	0.03	0.6	0.01	0.9	0.09	0.205
20% events	0.03	0.7	−0.01	0.94	**0.13**	**0.1**
25% events	0.02	0.8	−0.01	0.88	0.04	0.54
30% events	0.05	0.53	0.05	0.45	**0.11**	**0.09**
NAWTD event occurrence						
5% events	**0.44**	**0.01**	0.17	0.25	0.19	0.201
10% events	**0.34**	**0.01**	0.14	0.25	0.08	0.51
15% events	**0.31**	**0.001**	0.08	0.38	0.02	0.85
20% events	**0.21**	**0.007**	0.01	0.88	0.03	0.7
25% events	**0.13**	**0.05**	0.01	0.86	−0.03	0.6
30% events	**0.11**	**0.045**	0.03	0.64	0	0.99

Bold numbers indicate trends that are significant at the 10% level.

To assess the sensitivity of our results to the choice of the data set, we compare trends from three other temperature data sets (Table 2 and Figure S1). Like NCEP-NCAR R1, PRISM—which is the only observational data set based entirely on ground observations—exhibits statistically significant increases in dipole event frequency for all dipole event categories. Further, the magnitude of trends in western U.S. temperature and in the fraction of the region experiencing extremes is similar between NCEP-NCAR R1 and PRISM. In contrast, there are considerable differences in the direction and magnitude of trends in western/eastern U.S. temperature, the fraction of the respective domains experiencing extremes, and the characteristics of NAWTD events across the four data sets. Although we find good agreement with the observation-based trends in NAWTD frequency, these differences in the other characteristics should be noted.

3.3. Relation to Trends in Large-Scale Atmospheric Circulation Patterns

We hypothesize that the detected increasing occurrence of extreme NAWTD events could be associated with the thermodynamic effects of enhanced radiative forcing or with changes in atmospheric circulation patterns that favor the advection of warm air into the western U.S. and/or cold Arctic air toward the eastern U.S. [*Horton et al*., 2015] or with some combination of the two.

We quantify these respective contributions by using Self-Organizing Maps (SOM) to categorize daily winter 500 mb circulation patterns into typical clusters (Figure S2). Based on the spatial correlation between the geopotential height anomaly composite for each cluster and the NAWTD circulation composite, we identify 6 of the 20 SOM clusters that most closely resemble the geopotential height composite pattern associated with the 15%-area dipole events (Figure 4). These six patterns have the highest number of NAWTD events associated with their occurrence: Although they collectively occur on less than one third of winter days (29 days per DJF season) (Figure 4m), together they account for >66% of historical NAWTD days (Figure 4n). Individually, the probability that the atmospheric pattern produces a NAWTD event is at least 20% for each of these six patterns (Figures 4d–4f and 4j–4l). (Of these six patterns, Node 3 has the highest spatial correlation NAWTD pattern (0.76) (Figure 4b) and ~39% of Node 3 pattern occurrences are associated with NAWTD event occurrences (Figure 4e).)

Despite spatial differences in their patterns, each of the six SOM patterns exhibits ridging near or over the western U.S. and troughing over the central or eastern U.S. (Figures 4a–4c and 4g–4i). Further, the remaining 14 clusters only account for 34% of the NAWTD occurrences and have negative or close-to-zero correlations

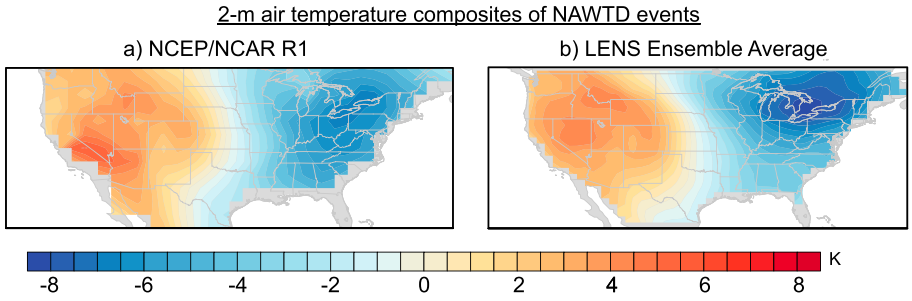

Figure 5. Model evaluation: Composites of daily average 2-m air temperature anomalies for all historical (1980–2015) 15% NAWTD events in (a) the NCEP/NCAR R1 and (b) the 35-member NCAR Large Ensemble (LENS) historical realizations.

with the NAWTD composite. We therefore conclude that these six SOM clusters represent atmospheric configurations that are most conducive to the NAWTD pattern (Figure 1b).

Collectively, the frequency of occurrence of these six "leading" atmospheric patterns has a positive trend corresponding to an increase of 5 days per season over the 36 year period, with 2013–2014 and 2014–2015 exhibiting among the highest seasonal occurrences of these patterns on record (Figure 4m, black line). However, the trend in total occurrence of these six patterns is not statistically significant (P-value = 0.4), meaning that the extent to which the observed increase in frequency of NAWTD events can be explained by changes in atmospheric pattern occurrence is inconclusive. Further, we also do not find any substantial trends in the persistence of these circulation patterns (Figure S3).

In contrast, there is a strong and highly significant trend (P-value = 0.02) in the production of NAWTD events, with the six leading patterns exhibiting an increase of 0.61 percentage points per year in the fraction of pattern occurrences that produce NAWTD events (Figure 4m, red line). This amounts to a 22 percentage point increase over 36 years ($0.61 \times 36 = 22\%$), which is an approximate doubling of the fraction of the pattern occurrences producing NAWTD events. Further, the increase in NAWTD occurrence has been more than twice as rapid for days with the six leading atmospheric patterns (0.27 NAWTD per year) than for days with the other 14 atmospheric patterns (0.11 NAWTD per year) (Figure 4n). This means that in recent years, mid-tropospheric dipole configurations have become more likely to produce dipole temperature extremes at the surface, and those patterns have been largely responsible for the increase in total dipole temperature occurrences.

Independent of changes in atmospheric pattern occurrence, the significant trend in the fraction of pattern occurrences that produce dipole events indicates that thermodynamic factors might have also changed the probability of extreme surface conditions. The probability of occurrence of dipole events associated with the occurrence of specific circulation patterns is influenced by the background thermal state of the atmosphere both locally and in remote regions from where these circulations advect air into the region. Thus, thermodynamic changes such as increased long-wave radiation or changes in surface conditions that alter near-surface air temperatures locally could have increased the likelihood of dipole events. For instance, seasonal warming in the western U.S. would likely contribute to an increase in dipole event occurrence even without an increase in the frequency of associated circulation patterns, provided that the air being advected into the eastern U.S. remains sufficiently cold to still produce cold extremes in the east. Similarly, advection of warmer air from over the tropical or eastern Pacific into the western U.S. and increased cool-air advection from Arctic by southward extension of the eastern trough could increase the probability of warm extremes in the west and cool extremes in the east [*Francis and Vavrus*, 2012; *Wang et al*., 2014; *Hartmann*, 2015].

3.4. Probability of NAWTD Events in Pre-industrial, Historical, and Future Climates

We examine the influence of different levels of climate forcing by comparing the simulated NAWTD frequency and intensity in the pre-industrial, historical, and 21st century climate of the NCAR single-model large single-model ensemble (LENS) simulations [*Kay et al*., 2014]. LENS is able to simulate the mean structure and magnitude of NAWTD events (Figures 5 and S4), as well as the magnitude of NAWTD occurrence and intensity during the historical period (Figure 6).

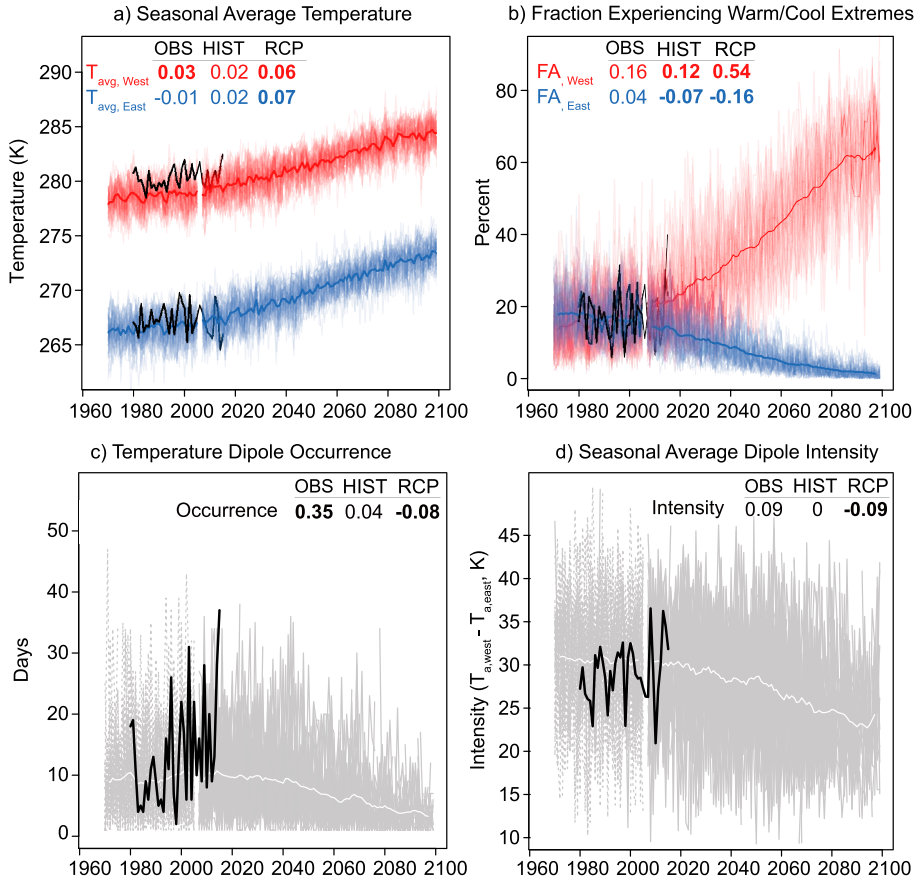

Figure 6. Historical and future trends: Historical (1920–2005) and RCP8.5 (2006–2100) 35-member LENS time series of winter (DJF) season (a) western and eastern domain average temperatures, (b) domain average land fraction in the west/east exceeding grid-cell warm/cool thresholds, (c) frequency of 15% NAWTD event occurrences, and (d) seasonal average intensity of 15% NAWTD events. NCEP/NCAR R1 data are the solid black line in all panels. The heavy red, black, and white lines are the 5 year moving average of the 35-member LENS ensemble mean. The numbers in each panel indicate the magnitude of the linear trend of each metric in the reanalysis (OBS) and the LENS ensemble average in historical (HIST) and RCP8.5 experiments. Trend magnitudes are bold if significant at the 5% level.

We first compare the observed trend with the ensemble of simulated trends during the historical period. The ensemble mean trend across the HIST LENS ensemble is positive for both the seasonal-mean western U.S. temperature and the fraction of the western U.S. experiencing extremes (Figures 6a and 6b), with the observed trend lying within the respective simulated range of trends in the historical simulations (Figures 7a and 7b). As a result, the historical ensemble average shows an increasing frequency of NAWTD events, consistent in direction with the observations, but with a lower magnitude (Figures 6c and 7c). The ensemble average does not show an increasing trend in NAWTD severity, although the observed positive trend lies within the simulated range (Figures 6d and 7d).

We find substantial evidence in the LENS simulations that anthropogenic warming has increased the likelihood of positive trends in NAWTD occurrence (Figure 7). Compared with the pre-industrial control, the historical climate simulations show a much greater likelihood of positive trends in the seasonal-mean western U.S. temperature and in the fraction of the western U.S. experiencing warm extremes (H2 P-value = 0.003; Figures 7a and 7b). For dipole events, the distribution of 36 year trends in the historical and pre-industrial climates is statistically distinguishable for NAWTD frequency but not NAWTD intensity (Kolmogorov-Smirnov test P-value is <0.001 and 0.62, respectively). A greater fraction of ensemble members exhibit a positive trend in NAWTD occurrence in the historical climate than in the pre-industrial climate, irrespective of the area threshold (Figure S5). For example, a positive trend in 15% area dipole events occurs in ~75% of historical realizations, compared with ~49% of 36 year periods from the PI control simulations (Figure 7c). The

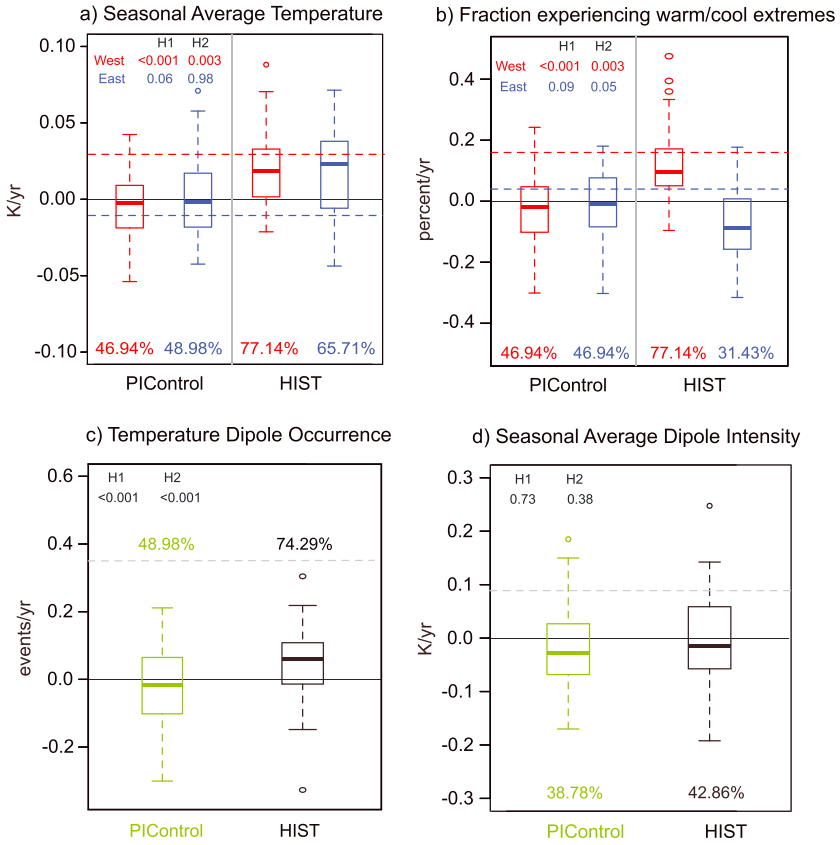

Figure 7. Trend attribution: Pre-industrial (PIcontrol) and historical (HIST) LENS simulations of 36-year winter season (DJF) trends in (a) western and eastern domain average temperatures, (b) domain average land fraction in the west/east exceeding grid-cell warm/cool thresholds, (c) frequency of 15% NAWTD event occurrences, and (d) seasonal average intensity of 15% NAWTD events. The box-whisker plots present the standard distribution percentiles (5th, 25th 50th, 75th, and 95th), while the open circles depict outlier trends. The dashed red and blue lines in Figures 7a and 7b and the grey lines in Figures 7c and 7d indicate the magnitude of the NCEP/NCAR R1 trends. Percentages of positive trends are indicated above/below box-whisker plots (see Table S1 for the fraction of these trends that are significant at the 5% level in the PIcontrol and HIST climates). *P*-values from binomial tests to assess—(H1) whether the likelihood of positive/negative trends is equal in the historical and pre-industrial climate and (H2) whether the likelihood of trends in the direction of observations (positive/negative) is higher in the historical climate relative to the pre-industrial climate, are indicated in the top left of each panel.

probability of three fourths of the historical members exhibiting positive trends due to natural variability is extremely low (H2 *P*-value <0.001), implying that historical climate change has significantly increased the likelihood of a positive trend in the occurrence of NAWTD events.

Finally, the median trend in dipole severity is higher in the historical than pre-industrial climate for the 10%, 15%, and 30% NAWTD events (Figure S5). However, the differences are relatively small, and we cannot reject the possibility that the difference in probability in the historical and pre-industrial climate is within the range of natural climate variability (Figure 7d). Taken together, our analysis therefore suggests that the observed historical increase in the frequency of NAWTD events may be attributable to human influence, but that natural variability is sufficiently large to mask any potential signal in NAWTD intensity.

We also find that continued increases in greenhouse gas concentrations in the 21st century are likely to increase temperatures in the western and eastern domains (Figure 6a). This warming reduces the fraction of the East below the cold threshold (Figure 6b), thereby reducing the frequency and intensity of extreme warm-West/cool-East events (Figures 6c and 6d). (For this calculation, we use the absolute warm and cold thresholds from the 1980–2000 baseline period to identify dipole events throughout the 21st century, as these represent the baseline climate variability to which people, infrastructure, and other systems are currently adapted.). The ensemble mean of NAWTD frequency and intensity show no statistically distinguishable

trends in the near-term but do exhibit statistically significant decreasing trends beginning in the mid-21st century (Figures 6c and 6d). The LENS ensemble therefore projects that despite the substantial variability that characterizes eastern U.S. wintertime temperatures, long-term global warming is likely to eventually decrease the occurrence and intensity of co-occurring wintertime warm-West/cool-East surface temperature extremes similar to those observed during recent winter seasons.

Note that our analysis does not necessarily suggest that the occurrence of the underlying high-amplitude mid-tropospheric wave pattern that characterizes these events will change in the future. Instead, we demonstrate that the simulated net effect of anthropogenically forced dynamic and thermodynamic changes yields an overall decrease in the frequency of the NAWTD surface temperature pattern during the 21st century. However, such changes in atmospheric circulation could occur in response to changing surface forcings, which could in turn influence the likelihood of large-scale atmospheric conditions favorable for NAWTD events. Efforts to understand the response of atmospheric circulation to climate forcing are therefore critical for constraining changes in the likelihood of extremes [*Shepherd*, 2014; *Horton et al*., 2015]. Future work will address possible 21st century changes in daily-scale atmospheric circulation patterns conducive to surface meteorological extremes in the United States.

The advantage of the large single-model ensemble is that it can constrain "irreducible" uncertainty arising from the model's simulation of internal climate variability by leveraging the large "sample size" created by the many ensemble members. However, we note some important caveats to consider in interpreting these results. First, the fact that the observed trends in dipole frequency and intensity fall within the upper tail of the distribution of trends simulated by the LENS historical ensemble (Figure 7) suggest that the model is not sufficiently sensitive to the historical forcing (if dipole events are indeed externally forced), that the true natural variability is stronger than the variability represented in the model, and/or that natural variability contributed substantially to the observed trend. The eventual availability of large ensembles of many different climate models will help to determine the precise contributions of anthropogenic forcings and natural variability to the observed trend. Second, although CESM has been shown to closely simulate the observed spatial structure and frequency of natural modes of variability such as ENSO and NAO that influence North American temperatures [*Z. Wang et al*., 2015], it is also possible that other remote forcings or processes that could modulate the occurrence of dipole temperature events are not well represented in the model (such as oceanic or land-atmosphere feedback). This is of particular interest since many global climate models, including CESM, underestimate trends in Arctic sea ice loss [*Stroeve et al*., 2012; *Swart et al*., 2015] and Eurasian snow cover [*Furtado et al*., 2015, 2016] and may not adequately capture spatiotemporal patterns of recent tropical Pacific warming [*Kosaka and Xie*, 2013; *Meehl et al*., 2014]. Since each of these hypothesized large-scale forcings (and their relevant interactions and teleconnections) [*Furtado et al*., 2015; *Trenberth et al*., 2015] are themselves likely influenced by human forcings [*Cubash et al*., 2013; *Funk and Hoell*, 2015], further evaluation of the model representation of such mechanistic linkages will help to further constrain the probability of extreme dipole temperature events in North America.

4. Discussion and Conclusions

We propose a metric that characterizes the spatial and temporal characteristics of high-impact daily-scale extreme surface temperature dipole events (NAWTD) that have been particularly prominent over North America in the winters of 2013–2014 and 2014–2015. We show that these events are associated with a well-defined, continental-scale pattern of atmospheric circulation anomalies extending across the mid-latitudes from the eastern Pacific to the western Atlantic. In addition, we also find large geopotential height anomalies in the high-latitudes, particularly in the East Siberian and Chukchi Seas regions.

The locations of these circulation anomalies complement the findings of previous studies linking the seasonal wintertime circulation anomalies over North America to processes occurring in geographically remote regions [*Cohen et al*., 2014; *Vihma*, 2014; *Hartmann*, 2015; *Overland et al*., 2015]. Substantial reductions in sea ice concentrations in the Barents-Kara Seas and Chukchi Seas, regions that have experienced warming in recent decades [*Deser and Teng*, 2008], have been linked to historical cold air outbreaks and extreme winter cold events over the Eurasia continent and North America [*Handorf et al*., 2015; *Kug et al*., 2015]. Additionally, the persistence of the anomalous ridge over the Pacific Northwest is indicative of a seasonal-scale circulation

anomaly, consistent with the hypothesized response of the atmosphere to forcing by Arctic sea ice loss [*Francis and Vavrus*, 2012; *Tang et al*., 2013; *Cohen et al*., 2014; *Overland et al*., 2015] and warm tropical West Pacific sea-surface temperatures [*Wang et al*., 2014; *Hartmann*, 2015]. It is also noteworthy that the interannual variability of NAWTD events appears to be much higher in the latter part of the record (2000–present) (Figure 2), a period during which there has been rapid and extensive autumn sea ice loss in parts of the Arctic, including in the East Siberian/Chukchi Seas region [*Stroeve et al*., 2012]. These results collectively suggest that investigating the interactions between daily- and seasonal-scale processes will improve our understanding of the mechanistic pathways through which different external forcings interact to affect the winter circulation patterns, thereby improving prediction of these high-impact events.

Daily-scale analysis of the historical record shows that the winters of 2013–2014 and 2014–2015 had an unprecedented number of NAWTD events and that the occurrence of such contrasting surface temperature extremes has increased substantially in recent years. Over the same period, we also find increases in the occurrence of daily-scale atmospheric circulation patterns similar to those linked to extreme dipole temperature events. This increase in favorable atmospheric circulation patterns combines with divergent regional mean temperature trends—namely, strong winter warming in the American West and weak cooling in the East—to produce significant increases in both the fraction of favorable atmospheric patterns that produce extreme surface temperature dipole events, and increases in the overall frequency of those dipole events.

Our analysis suggests that the observed positive trend in NAWTD occurrence is significantly more likely to occur under historical forcing than under the unperturbed pre-industrial forcing regime. In contrast, natural variability is sufficiently large to mask any potential signal in NAWTD intensity. Continued increases in greenhouse forcing are very likely to decrease the overall frequency of extreme surface temperature dipole events as warming of the East reduces the occurrence of extremely cold conditions. However, we note that a number of NAWTD events still occur in the mid-to-late 21st century (Figure 6c), in agreement with previous analyses indicating that even high greenhouse concentrations do not completely preclude the occurrence of individual severely cold winter events [*Vavrus et al*., 2006; *Kodra et al*., 2011; *Kodra and Ganguly*, 2014; *Scherer and Diffenbaugh*, 2014; *Screen et al*., 2014].

Our historical analysis finds robust changes in the warm-West/cool-East pattern over North America within the last 35 years, related to both historical surface warming and changes in the probability of extreme conditions associated with specific atmospheric circulation patterns. In addition, the LENS projections of decreasing NAWTD events in the 21st century are primarily related to the lower likelihood of crossing the baseline cold threshold in the eastern U.S. under high levels of greenhouse forcing. The change in direction of trends in NAWTD occurrence between the historical and future periods has important implications for managing the risk of extreme events over the current, near-term, and long-term time-horizons. Further, although our immediate emphasis is on particular surface temperature extremes in North America, our approach introduces a joint dynamical and statistical framework that could be generally applied for understanding the physical mechanisms driving changes in extremes in any region of the globe.

Acknowledgments

We thank the National Oceanic and Atmospheric Administration's NCDC for access to historical temperature and geopotential height data sets, PRISM Climate Group and University of Idaho for access to historical temperature data sets, and NCAR for access to the CESM LENS simulations. We also thank Nathaniel Johnson for providing us the Self-Organizing Maps algorithm. Our work is supported by the Lamont Doherty Postdoctoral Fellowship to D.S.; graduate fellowships from the Switzer Foundation and the ARCS Foundation to D.L.S.; Earth Institute Postdoctoral Fellowship to J.S.M.; US National Science Foundation grants DMS-CMG 1025465, AGS-1003823, DMS-1106642, and DMS-CAREER-1352656; and U.S. Air Force Office of Scientific Research grant award FA9550-13-1-0043 to B.R.; and NSF AGS CAREER grant 0955283 and DOE Integrated Assessment Research Program grant DE-SC005171 to N.S.D. Gridded 2 m temperatures, geopotential heights, meridional winds, and omega from the NCEP R1 and 2 m temperatures from the NCEP North American Regional Reanalysis (NARR) are available at the NOAA ESRL website (http://www.esrl.noaa.gov/psd/data/gridded/). Gridded temperatures from PRISM Climate Group and University of Idaho Metdata data sets are available at their respective websites (http://www.prism.oregonstate.edu/ and http://metdata.northwestknowledge.net/). All analysis scripts used in this study can be obtained by contacting Deepti Singh (dsingh@ldeo.columbia.edu).

References

Abatzoglou, J. T. (2013), Development of gridded surface meteorological data for ecological applications and modelling, *Int. J. Climatol.*, *33*(1), 121–131, doi:10.1002/joc.3413.

Bacon, J. (2015), Deadly snow, ice bring havoc to South, East, *USA Today*, 17th February.

Bao, M., and J. M. Wallace (2015), Cluster analysis of Northern Hemisphere wintertime 500-hPa flow regimes 1920–2014, *J. Atmos. Sci.*, doi:10.1175/JAS-D-15-0001.1.

Blackmon, M. L., J. M. Wallace, N.-C. Lau, and S. L. Mullen (1977), An observational study of the Northern Hemisphere wintertime circulation, *J. Atmos. Sci.*, *34*(7), 1040–1053, doi:10.1175/1520-0469(1977)034<1040:AOSOTN>2.0.CO;2.

Cattiaux, J., H. Douville, and Y. Peings (2013), European temperatures in CMIP5: Origins of present-day biases and future uncertainties, *Clim. Dyn.*, *41*(11–12), 2889–2907, doi:10.1007/s00382-013-1731-y.

Cohen, J., J. Jones, J. C. Furtado, and E. Tziperman (2013), Warm Arctic, cold continents: A common pattern related to Arctic sea ice melt, snow advance, and extreme winter weather, *Oceanography*, *26*(4), 150–160, doi:10.5670/oceanog.2013.70.

Cohen, J., et al. (2014), Recent Arctic amplification and extreme mid-latitude weather, *Nat. Geosci.*, *7*, 627–637, doi:10.1038/ngeo2234.

Comiso, J. C., C. L. Parkinson, R. Gersten, and L. Stock (2008), Accelerated decline in the Arctic sea ice cover, *Geophys. Res. Lett.*, *35*, L01703, doi:10.1029/2007GL031972.

Cubash, U., D. Wuebbles, D. Chen, M. C. Facchini, D. Frame, N. Mahowald, and J.-G. Winther (2013), Introduction, in *Climate Change 2013: The Physical Science Basis. Contribution of Working Group 1 to the Fifth Assessment Report of the Intergovermental Panel on Climate Change*, edited by T. F. Stocker et al., pp. 119–158, Cambridge Univ. Press, Cambridge, U. K., and New York.

Dawson, A., and T. N. Palmer (2015), Simulating weather regimes: Impact of model resolution and stochastic parameterization, *Clim. Dyn.*, *44*(7–8), 2177–2193, doi:10.1007/s00382-014-2238-x.
Deser, C., and H. Teng (2008), Evolution of Arctic sea ice concentration trends and the role of atmospheric circulation forcing, 1979–2007, *Geophys. Res. Lett.*, *35*, L02504, doi:10.1029/2007GL032023.
Diffenbaugh, N. S., D. L. Swain, and D. Touma (2015), Anthropogenic warming has increased drought risk in California, *Proc. Natl. Acad. Sci. U.S.A.*, *112*(13), 3931–3936, doi:10.1073/pnas.1422385112.
Ding, Q., J. M. Wallace, D. S. Battisti, E. J. Steig, A. J. E. Gallant, H.-J. Kim, and L. Geng (2014), Tropical forcing of the recent rapid Arctic warming in northeastern Canada and Greenland, *Nature*, *509*(7499), 209–212.
Driouech, F., M. Déqué, and E. Sánchez-Gómez (2010), Weather regimes—Moroccan precipitation link in a regional climate change simulation, *Global Planet. Change*, *72*(1–2), 1–10, doi:10.1016/j.gloplacha.2010.03.004.
Feldstein, S. B. (2000), The timescale, power spectra, and climate noise properties of teleconnection patterns, *J. Clim.*, *13*(24), 4430–4440, doi:10.1175/1520-0442(2000)013<4430:TTPSAC>2.0.CO;2.
Francis, J. A., and S. J. Vavrus (2012), Evidence linking Arctic amplification to extreme weather in mid-latitudes, *Geophys. Res. Lett.*, *39*, L06801, doi:10.1029/2012GL051000.
Franzke, C., S. B. Feldstein, and S. Lee (2011), Synoptic analysis of the Pacific-North American teleconnection pattern, *Q. J. R. Meteorol. Soc.*, *137*(655), 329–346, doi:10.1002/qj.768.
Funk, C. C., and A. Hoell (2015), The leading mode of observed and CMIP5 ENSO-residual sea surface temperatures and associated changes in Indo-Pacific climate, *J. Clim.*, *28*(11), 4309–4329, doi:10.1175/JCLI-D-14-00334.1.
Furtado, J., J. Cohen, A. Butler, E. Riddle, and A. Kumar (2015), Eurasian snow cover variability and links to winter climate in the CMIP5 models, *Clim. Dyn.*, 1–15, doi:10.1007/s00382-015-2494-4.
Furtado, J. C., J. L. Cohen, and E. Tziperman (2016), The combined influences of autumnal snow and sea ice on Northern Hemisphere winters, *Geophys. Res. Lett.*, *43*, 3478–3485, doi:10.1002/2016GL068108.
Griffin, D., and K. J. Anchukaitis (2014), How unusual is the 2012–2014 California drought?, *Geophys. Res. Lett.*, *41*, 9017–9023, doi:10.1002/2014GL062433.1.
Handorf, D., R. Jaiser, K. Dethloff, A. Rinke, and J. Cohen (2015), Impacts of Arctic sea ice and continental snow cover changes on atmospheric winter teleconnections, *Geophys. Res. Lett.*, *42*, 2367–2377, doi:10.1002/2015GL063203.
Hartmann, D. L. (2015), Pacific sea surface temperature and the winter of 2014, *Geophys. Res. Lett.*, *42*, 1894–1902, doi:10.1002/2015GL063083.
Holloway, J. L., Jr. (1958), Smoothing and filtering of time series and space, in *FieldsAdvances in Geophysics*, vol. 4, edited by H. E. Landsberg and J. Van Mieghem, pp. 351–389, Academic Press, New York.
Horton, D. E., N. C. Johnson, D. Singh, D. L. Swain, B. Rajaratnam, and N. S. Diffenbaugh (2015), Contribution of changes in atmospheric circulation patterns to extreme temperature trends, *Nature*, *522*(7557), 465–469, doi:10.1038/nature14550.
Intergovernmental Panel on Climate Change (2013), *Climate Change 2013: The Physical Science Basis. Contribution of Working Group 1 to the Fifth Assessment Report of the Intergovernmental Panel on Climate Change*, edited by T. F. Stocker et al., Cambridge Univ. Press, Cambridge, U. K., and New York.
Johnson, N. C. (2013), How many ENSO flavors can we distinguish?*, *J. Clim.*, *26*(13), 4816–4827, doi:10.1175/JCLI-D-12-00649.1.
Kalnay, E., et al. (1996), The NCEP/NCAR 40-Year Reanalysis Project, *Bull. Am. Meteorol. Soc.*, *77*(3), 437–471, doi:10.1175/1520-0477(1996)077<0437:tnyrp>2.0.co;2.
Kay, J. E., et al. (2014), The Community Earth System Model (CESM) large ensemble project: A community resource for studying climate change in the presence of internal climate variability, *Bull. Am. Meteorol. Soc.*, doi:10.1175/BAMS-D-13-00255.1.
Kodra, E., and A. R. Ganguly (2014), Asymmetry of projected increases in extreme temperature distributions, *Sci. Rep.*, *4*, 5884.
Kodra, E., K. Steinhaeuser, and A. R. Ganguly (2011), Persisting cold extremes under 21st-century warming scenarios, *Geophys. Res. Lett.*, *38*, L08705, doi:10.1029/2011GL047103.
Kohonen, T. (2001), *Self-Organizing Maps*, 3rd ed., Springer, Berlin.
Kosaka, Y., and S.-P. Xie (2013), Recent global-warming hiatus tied to equatorial Pacific surface cooling, *Nature*, *501*(7467), 403–407.
Kug, J.-S., J.-H. Jeong, Y.-S. Jang, B.-M. Kim, C. K. Folland, S.-K. Min, and S.-W. Son (2015), Two distinct influences of Arctic warming on cold winters over North America and East Asia, *Nat. Geosci.*, *8*(10), 759–762.
Lee, J., S. Li, and R. Lund (2014), Trends in extreme U.S. temperatures, *J. Clim.*, *27*(11), 4209–4225, doi:10.1175/JCLI-D-13-00283.1.
Lee, M.-Y., C.-C. Hong, and H.-H. Hsu (2015), Compounding effects of warm sea surface temperature and reduced sea ice on the extreme circulation over the extratropical North Pacific and North America during the 2013–2014 boreal winter, *Geophys. Res. Lett.*, *42*, 1612–1618, doi:10.1002/2014GL062956.
Meehl, G. A., H. Teng, and J. M. Arblaster (2014), Climate model simulations of the observed early-2000s hiatus of global warming, *Nat. Clim. Change*, *4*(10), 898–902.
NOAA (2015), State of the Climate: National Overview for February 2015.
Overland, J., J. A. Francis, R. Hall, E. Hanna, S.-J. Kim, and T. Vihma (2015), The melting Arctic and midlatitude weather patterns: Are they connected?*, *J. Clim.*, *28*(20), 7917–7932, doi:10.1175/JCLI-D-14-00822.1.
Petoukhov, V., S. Rahmstorf, S. Petri, and H. J. Schellnhuber (2013), Quasiresonant amplification of planetary waves and recent Northern Hemisphere weather extremes, *Proc. Natl. Acad. Sci. U.S.A.*, *110*(14), 5336–5341, doi:10.1073/pnas.1222000110.
PRISM (2015), PRISM Climate Group, Oregon State University, Available from: http://prism.oregonstate.edu (Accessed 1 March 2015).
Scherer, M., and N. Diffenbaugh (2014), Transient twenty-first century changes in daily-scale temperature extremes in the United States, *Clim. Dyn.*, *42*(5–6), 1383–1404, doi:10.1007/s00382-013-1829-2.
Screen, J. A., C. Deser, and L. Sun (2014), Reduced risk of North American cold extremes due to continued Arctic sea ice loss, *Bull. Am. Meteorol. Soc.*, *96*(9), 1489–1503, doi:10.1175/BAMS-D-14-00185.1.
Shepherd, T. G. (2014), Atmospheric circulation as a source of uncertainty in climate change projections, *Nat. Geosci.*, *7*(10), 703–708.
Singh, D., M. Ashfaq, R. Mei, D. E. Horton, N. Johnson, B. Rajaratnam, M. Tsiang, and N. S. Diffenbaugh (2014a), 2013 severe flooding in northern India in June 2013: Quantifying the likelihood of extreme June precipitation in the current and pre-industrial climates, "*Explaining Extrem. Events 2013 from a Clim. Perspect*, *Bull. Am. Meteorol. Soc.*, *95*(9), S58–61.
Singh, D., M. Tsiang, B. Rajaratnam, and N. Diffenbaugh (2014b), Observed changes in extreme wet and dry spells during the South Asian summer monsoon season, *Nat. Clim. Change*, *4*(6), 456–461, doi:10.1038/nclimate2208.
Stroeve, J. C., V. Kattsov, A. Barrett, M. Serreze, T. Pavlova, M. Holland, and W. N. Meier (2012), Trends in Arctic sea ice extent from CMIP5, CMIP3 and observations, *Geophys. Res. Lett.*, *39*, L16502, doi:10.1029/2012GL052676.
Swain, D. L., M. Tsiang, M. Haugen, D. Singh, A. Charland, B. Rajaratnam, and N. S. Diffenbaugh (2014), The extraordinary California drought of 2013/2014: Character, context, and the role of climate change, *Bull. Am. Meteorol. Soc.*, *95*, 3–7.

Swain, D., D. Horton, D. Singh, and N. S. Diffenbaugh (2016), Trends in atmospheric patterns conducive to seasonal precipitation and temperature extremes in California, *Sci. Adv.*, *2*(4), doi:10.1126/sciadv.1501344.

Swart, N. C., J. C. Fyfe, E. Hawkins, J. E. Kay, and A. Jahn (2015), Influence of internal variability on Arctic sea-ice trends, *Nat. Clim. Chang.*, *5*(2), 86–89.

Tang, Q., X. Zhang, X. Yang, and J. A. Francis (2013), Cold winter extremes in northern continents linked to Arctic sea ice loss, *Environ. Res. Lett.*, *8*(1), 014036, doi:10.1088/1748-9326/8/1/014036.

Trenberth, K. E., J. T. Fasullo, and T. G. Shepherd (2015), Attribution of climate extreme events, *Nat. Clim. Change*, *5*, 725–730.

Vavrus, S., J. E. Walsh, W. L. Chapman, and D. Portis (2006), The behavior of extreme cold air outbreaks under greenhouse warming, *Int. J. Climatol.*, *26*(9), 1133–1147, doi:10.1002/joc.1301.

Vihma, T. (2014), Effects of Arctic sea ice decline on weather and climate: A review, *Surv. Geophys.*, *35*(5), 1175–1214.

Wang, S.-Y. S., W.-R. Huang, and J.-H. Yoon (2015), The North American winter "dipole" and extremes activity: A CMIP5 assessment, *Atmos. Sci. Lett.*, doi:10.1002/asl2.565.

Wang, S.-Y. Y., L. Hipps, R. R. Gillies, and J.-H. H. Yoon (2014), Probable causes of the abnormal ridge accompanying the 2013–2014 California drought: ENSO precursor and anthropogenic warming footprint, *Geophys. Res. Lett.*, *41*, 3220–3226, doi:10.1002/2014GL059748.

Wang, Z., Y. Li, B. Liu, and J. Liu (2015), Global climate internal variability in a 2000-year control simulation with Community Earth System Model (CESM), *Chin. Geogr. Sci.*, *25*(3), 263–273, doi:10.1007/s11769-015-0754-1.

Yoon, J.-H., S.-Y. S. Wang, R. R. Gillies, L. Hipps, K. Ben, and P. J. Rasch (2015), Extreme fire season in California: A glimpse into the future?, *Bull. Am. Meteorol. Soc.*, *96*(12), 5–9.